Single cell tomography of bacterial cells

Gideon Carmon

Abstract

In this study we will apply the Computerized Tomography (CT) technique on a single cells system, in order to obtain three dimensional images of protein structures within bacteria. An optical tweezers system will be used to trap a single bacterium, and to align it in different orientations for the CT imaging. Fluorescence will be used to mark specific proteins of the bacteria. This system setup will allow us visualize the spatial configuration of different proteins in the cells and follow its dynamic and evolution.

Contents

1. Scientific background

1.1 Optical tweezers

Optical tweezers can trap small objects ranging in size from few nanometers [1] to tens of micrometers and exert forces of up to 100pN. These ranges are suitable for exerting forces on biological and macromolecular objects and for measuring their responses. Since their invention in 1986, optical traps have been used in a wide range of studies in biology and physics, to trap dielectric spheres, viruses, bacteria, living cells, organelles, small metal particles and DNA strands. In biology research, optical trapping is used to study the forces exerted by molecular motors such as kinesin and dynein [2, 3], to manipulate live sperm cells [4, 5], measure their swimming forces [6] and to examine the mechanical properties of microtubules, actin filaments, and DNA bio-polymers [7–11]. On larger scales, optical tweezers are used for selecting individual microbes from heterogeneous populations. Their ability to transport cells have led to clinical applications as *in vitro* fertilization [12]. In the physical sciences, optical tweezers are used in classical statistical mechanics research to study the macromolecular interactions in solution [13], phase transitions and crystallization of random 2D colloidal suspension to a colloidal crystal [14] and to measure the entropic forces which control the motion of colloidal particles at passive surface microstructures [15].

Recent advances in physical optics enabled the broadening of the optical tweezers applications. For example a single rapidly scanned optical tweezer can simultaneously trap multiple particles [16, 17]. Modifying the optical tweezers' wavefront enables, among other things, to apply a torque on a trapped object. A wide variety of methods have been developed to allow the rotation and alignment of trapped objects [18–25], some by wave front modifications and others by scanned traps.

1.2 Three dimensional light microscopy imaging

Over the last decades, the development of powerful imaging techniques contributed significantly to biological studies. In particular, new methods in light microscopy that provide the potential to image the dynamics of biological events contributed significant tools for researches. Optical sectioning techniques allow three dimensional information to be obtained from living specimens noninvasively. Nomarski imaging is a relatively simple technique that uses refractive index to produce contrast [26]. The development of Laser Scanning Confocal

Microscopy (LSCM) provided a non destructive method for acquiring high contrast, three dimensional data with high resolution. Recently, multiphoton microscopy, in which NIR radiation is used to generate images without the use of a pinhole, restricts photobleaching and is potentially less damaging to living specimen when compared to visible and UV light [27]. An increasing number of biological and material science applications have been developed using LCSM . Optically transparent organic and inorganic materials are well suited for LSCM structures characterization. Non transparent materials may be imaged in reflection mode to create 3D surface images without the use of coating or other destructive sample preparations. For biological samples, fluorescent antibodies and probes are applied to derive specific chemical and biological information.

1.3 Protein structures associated with cell division

Most prokaryote cells, such as the rod shaped *Escherichia coli* (*E. coli*) bacteria, divide by a process called binary fission. In this process one cell gives rise to two identical daughter cells. During the growth of *E. coli* a septum forms at the center of the cell, which gradually shrinks to perform the cell separation. This seemingly simple event involves spacial and temporal controls that function to coordinate the physiological status of the cell, the replication of the genetic information (chromosomes), and chromosomal segregation, with cellular division.

Among dozens of different proteins that participate in the cell division process, at least nine are known to be required for proper septation, and to localize at the division plane during septation [28–30]. From this group, FtsZ is the first to assemble [31]. This tubulin-like protein, is polymerized in the presence of GTP to form a ring-like structure at midcell which is connected to the cytoplasmic membranee [28, 32]. Stricker *et al.* [33] used Fluorescence Recovery After Photobleaching (FRAP) to show that the Z-ring is an extremely dynamic structure, continually exchanging subunits with a cytoplasmic pool.

Following the assembly of FtsZ, additional division proteins are recruited into the Z-ring in sequential order [34], to form the divisome structure which carries out the cell division process. Unlike FtsZ, most of the division proteins are found in limited concentrations in the cell. For some proteins, there are not enough molecules to cover the circumference of the cell. Therefore, the divisome structure is believed to be divided into subunit assemblies, positioned at equidistant locations along the Z-ring. Further study is needed to confirm this

view of the divisome organization.

Another group of proteins involved in cell division is that of the Min proteins. The MinCDE proteins of *E. coli* are required for proper placement of the division septum at midcell. The site selection process requires rapid oscillations (with cycle period of a few minuets) of the proteins distribution from pole to pole. Even though these proteins play no apparent cytoskeletal role, they are organized into membrane-associated structures that coil around the cell between the two cell poles [35]. It has been proposed that the Min proteins configuration is part of the same coiled structure of the sytokeletal-like MreB protein, which was found to be essential for maintaining the rod shape of *E. coli* [36]. However, whereas the Min coils are observed in similar structures within different cells, the MreB seems to vary in density, number of loops in the coil structure, and location along the cell. These observations suggest that there is no common structure for Min and MreB proteins. Another suggestion is that MreB and the MinCDE proteins might be associated with a common structural element at some stage in their history. At the present, there is not enough experimental evidence to confirm either of those suggestions and further study is needed.

Rothfield *et al.* [35] observed that when the majority of the Min proteins are found at one pole, low concentration coiled Min structures are located in the other half of the cell, in contrary to what has been expected. Since the structures on opposite sides were found to be wound in opposite directions, it is likely that there are two separate helical constructions rather then one coil that stretches from one pole of the cell to the other. It is believed that the coil in the other half of the cell plays a role in the Min proteins dynamics. One suggested scenario is that MinD molecules that are released from the disassembling polar zone directly associate with a membrane associated helical framework at the opposite half of the cell to form a new polar zone. Another possibility is that MinD molecules initiate nucleation of coiled strands at the opposite pole, and the helical framework guides the growth of the new structure.

By observing the creation of a new polar zone using time-lapse microscopy with sufficient temporal resolution, it will be possible to distinguish between two possible scenarios: 1. organized nucleation and 2. random association of the MinD molecules along the helical framework.

2. Experimental methods

The experimental setup is based upon an optical microscope (Olympus IX70), to which we add an optical tweezers system and an intensified CCD camera (IPentaMAX). A laser beam (IR laser diode λ=830nm) is focused through the microscope objective (Olympus 100X, 1.3 NA oil immersion) in order to generate an optical trap in the sample. Trap oscillations are achieved via a galvanometric mirror located at a conjugate plane to the objective back aperture. System setup is shown in Fig. 1. Fluorescence will be used to illuminate the desired proteins in the bacteria. Image analysis requires high resolution tracking algorithms developed in previous work [37].

2.1 Optical tweezers

The optical tweezers system commonly used today originally reffered as *single beam gradient force optical trap*, was developed by Arthur Ashkin [38] in 1986. Such optical trap is formed by a single laser beam, strongly focused via a microscope high NA objective lens. A dielectric particle near the objective focal plane experiences trapping forces due to the momentum transfer from photons scattered by the particle. Such force may be decomposed into two components, namely scattering force and gradient force. The scattering force is generated by the photon flux that is simply pushing the particle in the direction of light propagation. While the scattered light goes in all directions, the incident light has a well defined momentum vector. As a result the fraction of light which is absorbed by the particle, and the fraction that is scattered backward, will generate a net force acting on the particle in the direction of light incidence. In order to understand the origin of the backward gradient force, both radially and axially, it is more convenient to examine the extreme cases of Mie particle (r$\gg \lambda$) and Raleigh particle (r$\ll \lambda$), where r is the particle dimension and λ is the laser wavelength. In the Mie regime, Ashkin used ray optics to describe the optical momentum transfer of the particle [39] . Qualitative description of the radial force is given in Fig.2.

A sphere with index of refraction n_H is placed off the beam axis, in a medium, e.g. water, of lower index n_L ($n_L < n_H$). Consider two rays, a and b, situated symmetrically about the sphere axis B. The Gaussian profile of the beam causes the intensity of a to be larger than that of b. Each beam undergoes reflection and refraction at both faces of the sphere, which leads to forces acting on the photons by the sphere. The reaction force that acts on

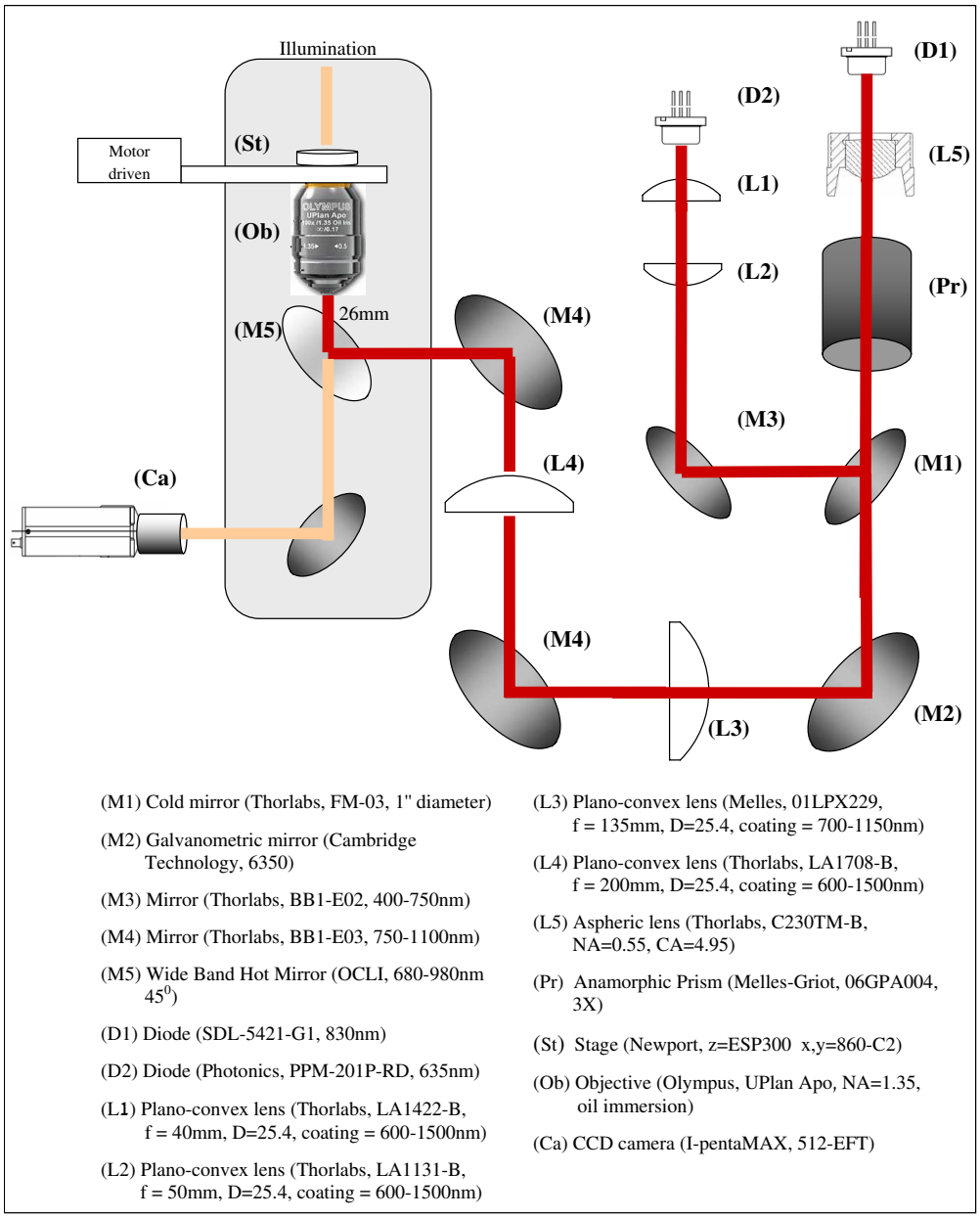

FIG. 1: System sketch

the sphere will be in the opposite direction, as illustrated in Fig. 2 by F_D and F_R. The radial components of F_D^i and F_D^o are larger than that of F_R^i and F_R^o, which cancel each other radially to first order. The z component of all forces are in the positive direction. The forces exerted by the b ray will have positive Z components as well, and opposite and weaker radial components. Thus the net force will be in the -r and +z directions for this situation.

The A' beams that emerge from the opposite side of the sphere are refracted (as can be seen from Fig. 3a), and thus generate a force on the particle. If we consider the direction of the resulting forces F_A, we see that there is a net backward force towards the beam focus.

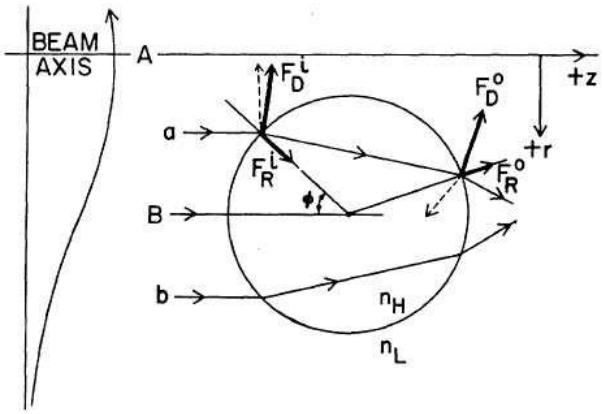

FIG. 2: A bead with high refraction index is placed off the axis of the TEM_{00} laser. F_D and F_R are the forces due the refraction and reflection of the beams, respectively. The i index represents the input point of the beam and o represents the output. The net force is in the -r and +z directions.

It is evident from the figure that this force is strongly dependent on the convergence of the beam. Fig. 3a represents the axial gradient force achieved by strongly focusing the light beam.

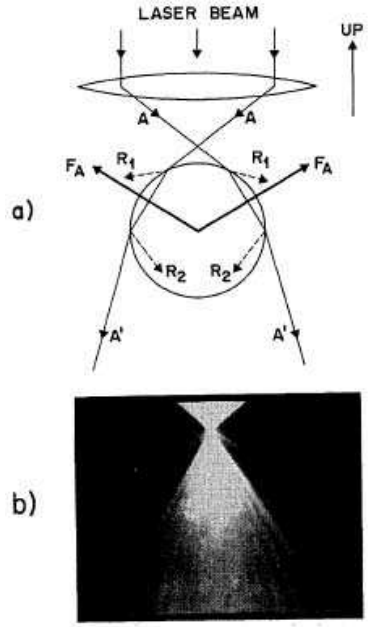

FIG. 3: a) A diagram showing the refraction of highly convergent rays by a bead positioned below the focus. b) Photograph, taken in fluorescence, of a 10μm sphere trapped in water, showing the paths of the incident and scattered light rays. The figure was taken from Ref. [39].

In the case of strong enough focusing, this backward gradient force will overcome the scattering force to achieve axial trapping, which together with the radial trapping described

above forms a three dimensional trap. In the Raleigh regime, the bead is treated as an induced electrical dipole. The trapping forces are formed by the inhomogeneous electrical field (the laser beam itself) applied on the particle. Such a non uniform field generates a force acting on the dipole, which is proportional and pointed in the direction of field gradient. For the wide range of objects that lie between the two extreme cases discussed above, such as a cell that is few microns long, trapped in an IR laser ($\lambda \simeq 0.8\mu$m), there's no simple model that describes the trapping forces. A more complete electromagnetic theory is needed in order to cover this range of particle sizes.

2.2 Optical alinement of a trapped cylindrical micro-object

In 1987 Arthur Ashkin *et al.* reported [40] that single living cells can be trapped and manipulated by IR optical tweezers. He observed the reproduction of E. coli bacteria and Yeast cells within a high power trap, indicating that no optical damage occurs under the influence of the laser. While stiff traps were capable of moving the bacteria with high velocities within the sample, its orientation was fixed along the laser propagation and could not be manipulated by the single trap. A few years later, Visscher *et al.* managed to control the orientation of elongated micro-objects [18]. By combining a Confocal Scanning Laser Microscope with an XY galvanometric mirror, he stirred an optical trap in a cyclic manner between a few fixed points in the microscope sample. A complete three dimensional control of the trap points was achieved by simultaneously moving the galvanometric mirror and one of the microscope objectives. When the scan repetition rate was higher then the mechanical response cut-off frequency, each point acted as an independent optical trap [16]. This enabled the orientation of irregularly shaped and relatively large structures which could not be oriented by just one trap. For example, an *E. coli* filament of $\simeq 20\mu m$ was captured by three traps of IR laser. This allowed a complete 3D control of the bacteria orientation. Although the orientation of smaller filaments in a single optical trap was observed, it could not be done in a controlled way.

R. C. Gauthier performed a ray optics theoretical investigation of the trapping force and torque applied on cylindrical mirco-objects [41]. In his model, the incident beam consists of a Gaussian intensity profile treated as a stream of photons that may transfer momentum to the cylinder when they are refracted and reflected at the cylinder interface.

The momentum transferred to the cylinder from a single photon reflected (r) and refracted

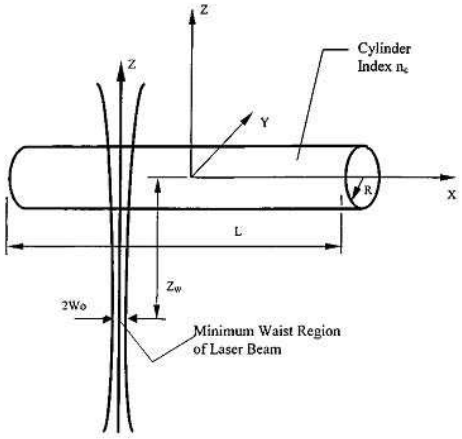

FIG. 4: A cylindrical micro-object of length L and radius R oriented along the x axis. The incident laser beam is directed along the z axis and comes to a focus at a distance z_w before passing the plane containing the cylinder axis.

(t) at an interaction point is given by:

$$d\mathbf{P}_r = \hbar\frac{2\pi}{\lambda}n_{in}\left[(l_0 - l_r)\hat{x} + (m_0 - m_r)\hat{y} + (n_0 - n_r)\hat{z}\right] \tag{1}$$

$$d\mathbf{P}_t = \hbar\frac{2\pi}{\lambda}n_{in}\left[(l_0 - n_{rel}l_t)\hat{x} + (m_0 - n_{rel}m_t)\hat{y} + (n_0 - n_{rel}n_t)\hat{z}\right] \tag{2}$$

where $(l_0, m_0, n_0), (l_r, m_r, n_r)$ and (l_t, m_t, n_t) are the incident, the reflected and the refracted photon direction cosines. n_{in} is the index of refraction of the medium in which the incident photon propagates and n_{rel} is the relative index of refraction between the transmitted side and the incident side of the interface.

The net force applied on the cylinder, by Newton second law, equals to the transferred photon momentum, taken over time interval dt, and is given by:

$$\mathbf{F} = \sum_i d\mathbf{F}_i = \sum_i N_i\left[Rd\mathbf{P}_r + (1-R)d\mathbf{P}_t\right] \tag{3}$$

where N_i is the photon flux, R is the reflection coefficient and $d\mathbf{F}_i$ is the force element at point i. The sum is over all the points of intersection. When the incident beam central axis is not aligned with the symmetry axis of the cylinder, a torque is generated. The torque can be obtained from:

$$\tau = \sum_i d\tau_i = \sum_i \mathbf{r}_i \times d\mathbf{F}_i \tag{4}$$

where $\mathbf{r}_i$ is a position vector pointing from a reference point to the i'th interaction point.

The force acting on the cylinder was numerically estimated for various bacteria lengths. The result exhibits 3D trapping forces, in agreement with previous experimental observations. Stable orientations were found by the requirement that the torque acting on the cylinder is both zero and restoring (turns the cylinder back to the stable orientation if it is turned to other direction). Stable trapping directions for various bacteria lengths are presented in Fig. 5. Most of the cylinders are found to be oriented such that their longest diagonal is closely aligned with the laser propagation axis.

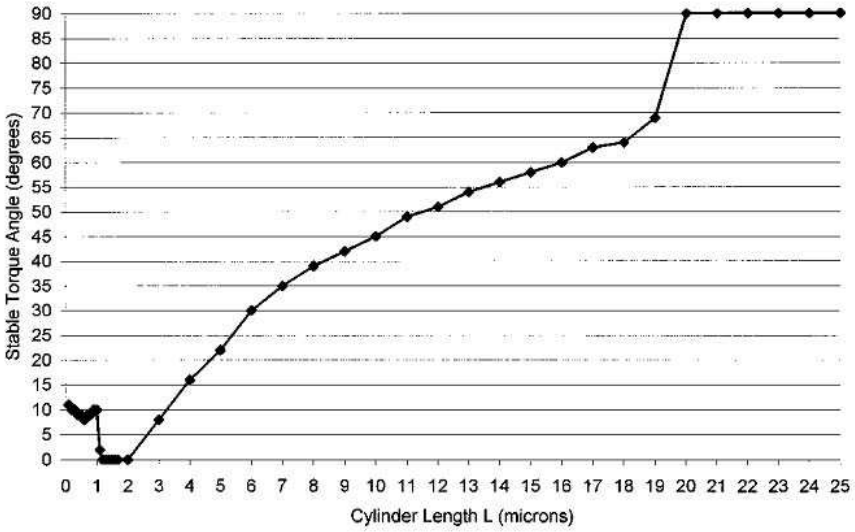

FIG. 5: Stable alignment angle versus cylinder length L where $R = 5\mu m$. Diamonds represent calculated points. The angle is between the z axis and the cylinder main axis

Experimental measurements of the cylindrical objects' orientation angle found to be in good agreement with the theoretical model [42].

In order to control the orientation of a trapped bacteria we developed a new method. Although our technique resembles that of Visscher *et al.* [18], it is based upon a much simpler setup.

We used a galvanometric mirror in the optical path of the trapping laser to oscillate a single optical trap in a plane perpendicular to the laser beam propagation axis. When the oscillations frequency was around 100Hz, the trap force was averaged along the oscillation amplitude to form an effectively elongated trap. A trapped cell was then aligned in a particular orientation. By varying the oscillations amplitude, we managed to control the alignment of the bacteria, through the whole range from z (corresponding to zero amplitude) to x (corresponding to bacterium length amplitude) axis alignment ($\theta = 90^o$ and $\theta = 0^o$, respectively). In order to determine the trapping angle for a certain orientation, we fixed a

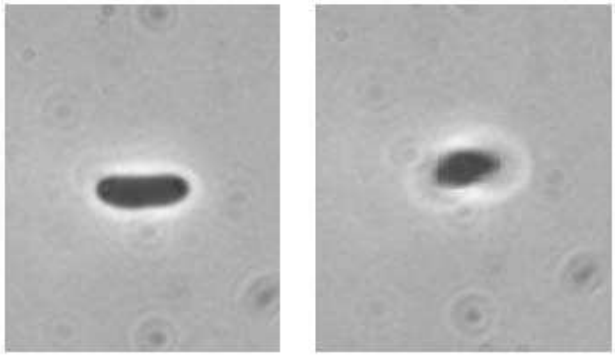

FIG. 6: An *E. coli* bacterium trapped in an oscillating optical tweezer. Left: Bacterium lies horizontally along the x axis since the oscillations amplitude is similar to the length of the cell. Right: Bacterium oriented at 50^0 with respect to the z axis. Oscillations amplitude is smaller than the length of the cell.

bacterium to the glass surface of the sample. The microscope stage was then moved in steps of $0.3\mu m$ in the z axis direction, from $z = -1.2\mu m$ to $z = +1.2\mu m$, where $z = 0$ is the focal plane of the objective. In each position the bacteria was imaged in phase contrast objective, to form a *height library*, as shown in Fig. 7.

The intensity profile along the symmetry axis of the bacteria in each frame was calculated. The intensity profile of the aligned bacteria was compared to the height library profiles. As can be seen in Fig. 8, each side of the profile was examined independently, in order to determine to which frame in the library it is most similar. Once this was determined, the orientation angle of the bacteria was calculated by simple geometry.

2.3 Computerized tomography

Tomography refers to the cross sectional imaging by illuminating an object from many different directions, followed by three dimensional reconstruction. This method was first applied in medical applications and it enabled doctors to view high resolution 3D images of internal organs with minor risk to the patients health. The first medical application used x-ray to form images of tissues based on their x-ray attenuation coefficient. Additional methods were invented later, using radioactive isotopes, ultrasound waves and magnetic resonance.

In the following the mathematical basis of non-diffracting source Computerized Tomography (CT) is introduced. In order to keep the arguments and calculations tractable, the

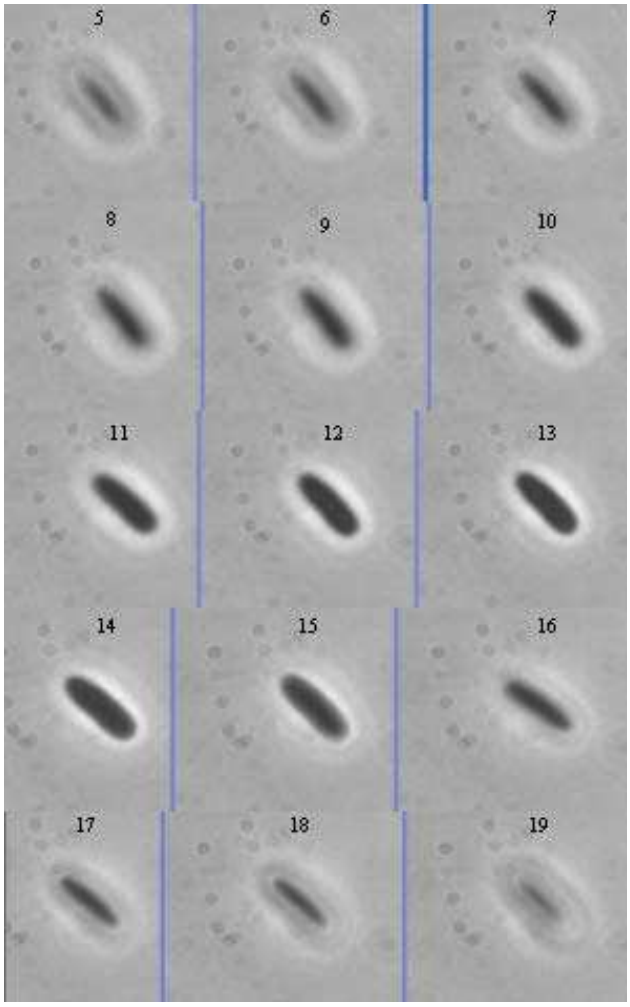

FIG. 7: Height library frames of an *E. coli* bacterium. The first frame (No. 5) was taken far below the focal plane of the objective. Each of the following frames were taken at a distance of $0.3\mu m$ in the upward direction from the previous frame. The focal plane is estimated to lie between frames 13 and 14.

analysis is presented for a 2D object. Even though the generalization to 3D is geometrically complex, the method fundamentals are similar to those in the 2D analysis.

When a two dimensional object is illuminated by parallel rays, the decay of the radiation due to absorption by the object is given by:

$$I_\theta(t) = I_0 exp\left[-\int_{(\theta,t)line} \mu(x,y)ds\right] \tag{5}$$

where t is a coordinate along the detectors array, s is a coordinate along the axis of the ray and the (θ, t) line definition is described in Fig. 9. The function μ(x,y) is the attenuation coefficient which is assumed to be proportional to the mass density of the object.

We can now replace the line integral with a surface integral by introducing Dirac delta

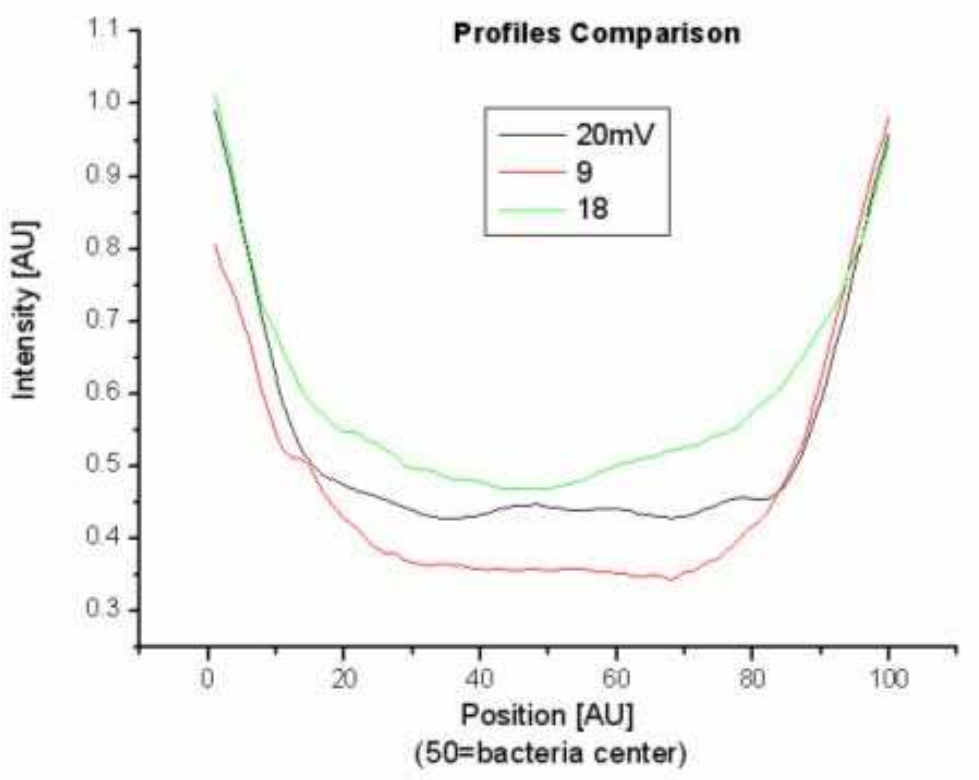

FIG. 8: Intensity profiles of the trapped bacterium shown in Fig. 6 (Black), library frame No. 9 (red) and library frame No. 18 (green). Note the matching of the trapped bacterium profile with frame No. 18 on the left and with frame No. 9 on the right. The trapping angle was estimated to be 50^o.

function to obtain the Radon Transform formula:

$$P_\theta(t) = \int_{-\infty}^{\infty}\int_{-\infty}^{\infty} \mu(x,y)\delta(xcos\theta + ysin\theta - t)dxdy \tag{6}$$

where the projection P is related to the intensity by the relation $P_\theta(t) \equiv log\frac{I_0}{I_\theta(t)}$. Given the line projection data at different orientations θ, it is possible to reconstruct the original image. This is done by first Fourier transforming the projections set into the frequency domain. The Fourier Slice Theorem states that each 1D projection equals a slice of the original object 2D Fourier transform, oriented at the corresponding angle, as described in Fig. 10. It follows that in order to reconstruct the image, the next step is applying a 2D inverse Fourier transform on the combined projections in the frequency domain.

Although in practice more complications are introduced in the reconstruction both mathematically and conceptually (in addition to the three dimensional analysis required), the simple prescription described above represents the essence of tomography.

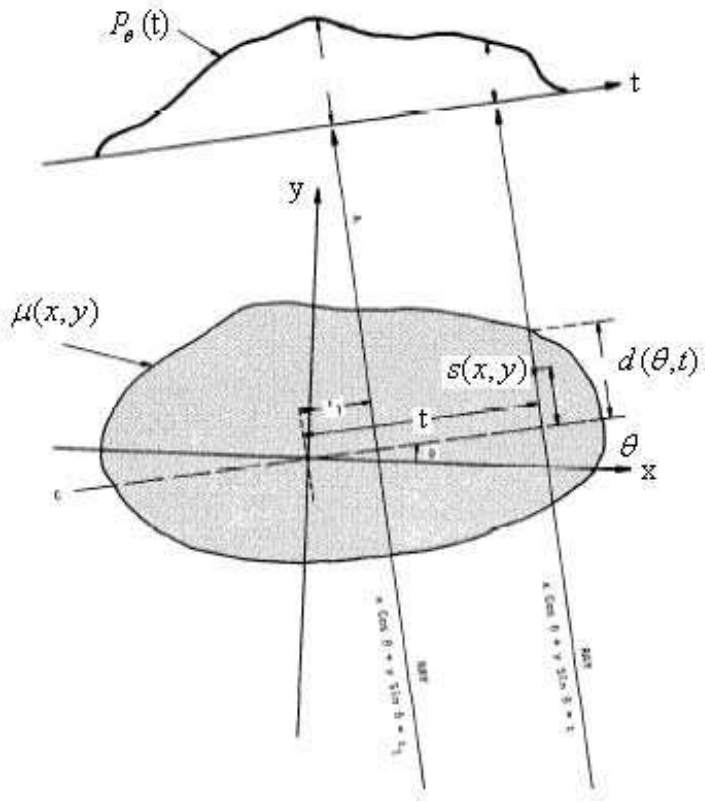

FIG. 9: An arbitrary shaped object is illuminated by parallel beams positioned at distance t from the object center, directed along the s axis which is tilted by angle θ with respect to the y axis. An array of sensors is positioned along the t axis to probe the light intensity decay due to absorption.

2.4 Single Photon Emission Computerized Tomography

Among different tomography methods and setups which are available and in use, the most relevant one for the current research is the Single Photon Emission Computerized Tomography (SPECT). Whereas in conventional x-ray tomography the attenuation coefficient of tissue is used to deduce information about biological objects, emission CT uses the decay of radioactive isotopes to image its distribution. The isotopes may be either inhaled or injected to the patient. Gamma-ray photons, which are a product of the nuclear decay, are collected outside the patient body and used as an indicator of the isotopes distribution. Since the emission process is assumed to be isotropic, in an ideal system where no absorption occurs, the number of photons that will reach a collimated detector will be proportional to the number of isotopes along a line pointing from the detector through the body in the direction of the collimator. Such line is denoted by R_2R_1 in Fig. 11. Therefore by replacing the attenuation coefficient with the mass distribution in the projection function definition, the

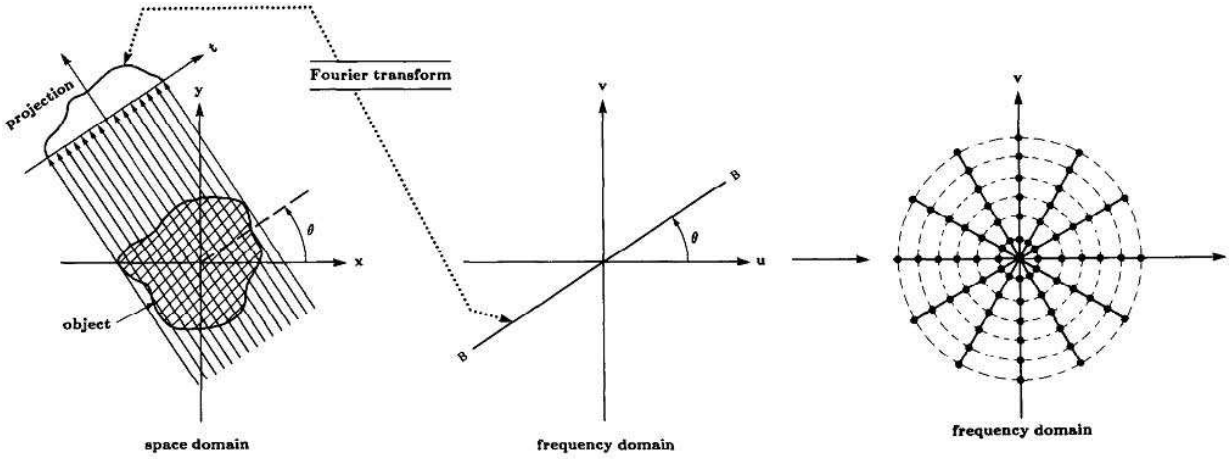

FIG. 10: A schematic description of the projections 2D reconstruction. Left: A projection line is probed at a certain tilting angle and its Fourier transform is then calculated. Center: The projection is placed in the frequency domain at the same orientation as it was taken at. Right: After a few iterations a two dimensional Fourier transform of the projections is formed. By the Fourier Slice Theorem the 2D transform formed in that manner equals the attenuation functions Fourier transform.

Radon Transform written in Eq. 6 is valid for photon emission tomography.

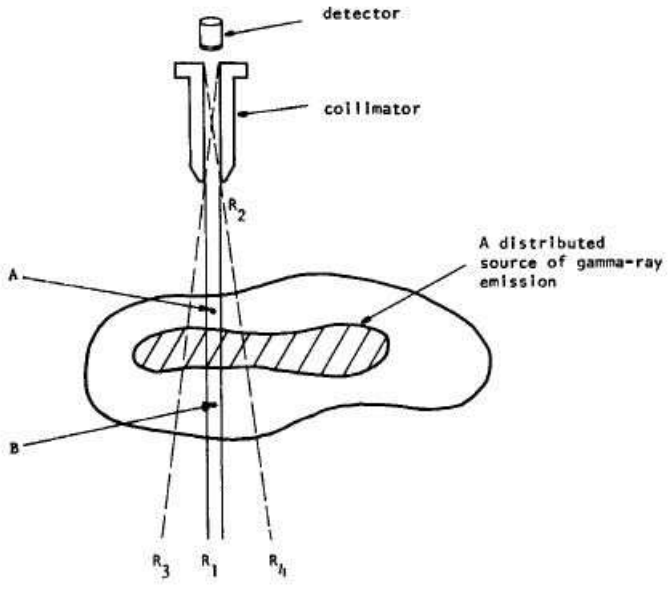

FIG. 11: In typical single emission tomography configuration a collimated detector is used for imaging a distribution of gamma-rays distributed source

A major difficulty in tomographic imaging of an emitting source is caused by the attenu-

ation that photons undergo during their travel from the emitting nuclei to the detector. The absorption will cause a point source positioned near the detector (denoted by A in Fig. 11) to have a stronger signal than a source that lies further away (such as point B in Fig. 11). The effect on the reconstruction image is most easily seen for a uniform distributed object. The peripheral areas of the object will appear to contain more isotopes than the center, as shown in the simulation results of Fig. 12.

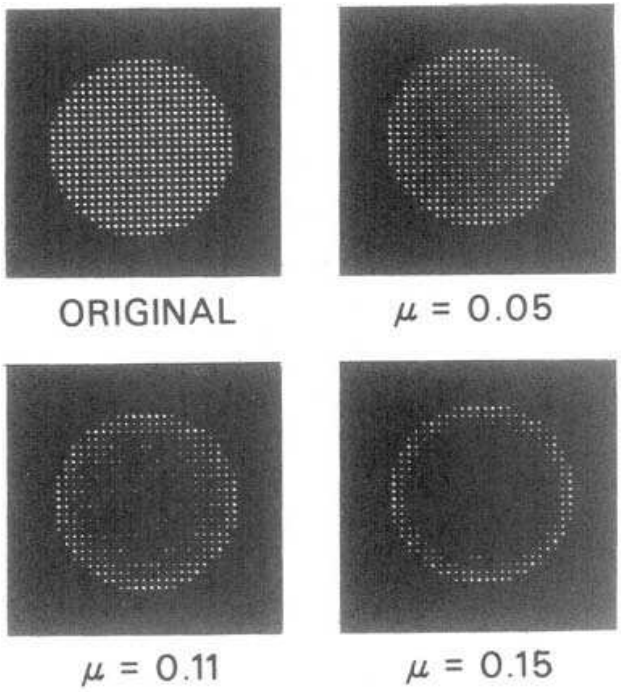

FIG. 12: Four reconstructions of Gamma-ray emitting disk for different values of the attenuation coefficients, μ.

The effect of radiation decay therefore requires a modification to the Radon transform of Eq. 6. Several methods were proposed [45–48] to handle attenuation compensation. One way is to add to each point source a corresponding weighting term in the sum of the contributions along each line:

$$P_\theta(t) = \int_{-\infty}^{\infty}\int_{-\infty}^{\infty} \mu(x,y) exp\left[-\mu(d-s)\right] \delta(xcos\theta + ysin\theta - t) dxdy \tag{7}$$

where d and s are described in Fig. 9. Tretiak and Metz have shown [49] that the attenuation compensation reconstruction of $\mu(x,y)$ is given by:

$$\hat{\mu}(r,\phi) = \int_0^{2\pi} \left[\int_{-\infty}^{\infty} S_\theta(rcos(\theta-\phi)-t)h(t)dt\right] exp\left[\mu r sin(\theta-\phi)\right] d\theta \tag{8}$$

where $S_\theta(t) = P_\theta(t)exp\,[\mu d]$ and provided h(t) fulfills certain conditions. An example of attenuation compensation applied to a real object is presented in Fig. 13.

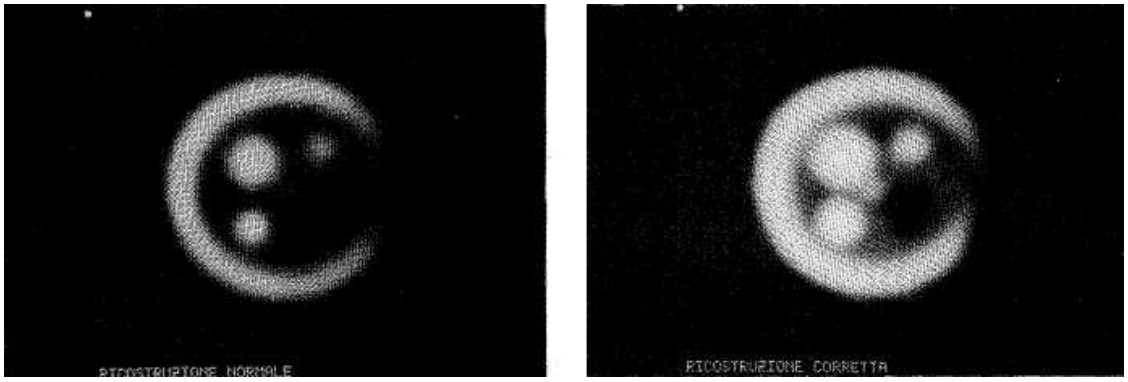

FIG. 13: On the left: Image reconstructed from real attenuated projections. On the right: Image reconstructed from real projections with attenuation compensation. Images were taken from Ref. 45.

2.5 Sufficient data collection

One the main concerns in tomography is to collect a sufficient amount of data so that the reconstruction would be of satisfying quality. We distinguish the spacial amount of data in each projection (spacing between successive detectors), from the number of projections captured at different orientations. For a given sensors array, the distance between two successive sensors is denoted by d. This length, d, introduces a frequency cutoff in the images frequency domain, denoted by f_c. This cutoff is determined by the Nyquist-Shannon sampling theorem [43, 44], and is given by: $\mathrm{f}_c = \frac{1}{2d}$. The space domain resolution is then determined to be $\simeq 2d$. The second factor to limit the resolution is the angle spacing between successive projections. In order to analyze the effect of this spacing let us refer to the frequency domain reconstructed image presented in Fig. 14. Note that the disk radius, f_c, is the highest frequency attainable. Since the tangential spacing varies with the radius, we shall focus on the worst case which is at the disk circumference. This spacing is given by $\mathrm{f}_t = \frac{1}{2d}\frac{\pi}{N_{proj}}$ where N_{proj} is the number of projections. On the other hand, the radial spacing is $\mathrm{f}_r = \frac{1}{dN_{detect}}$ where N_{detect} is the number of detectors (equals to the number of points along a radius). The criterion for the angle spacing between consecutive projections should be such that the tangential spacing will not exceed the fixed radial spacing. This provides the following relation:

$$\frac{N_{proj}}{N_{detect}} \simeq \frac{\pi}{2} \tag{9}$$

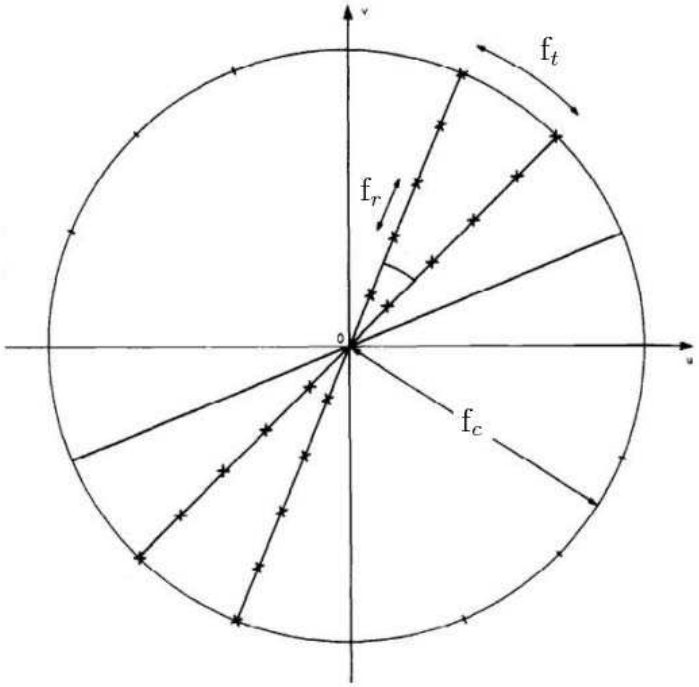

FIG. 14: Sketch of the reconstructed image in the frequency domain

2.6 The effect of noise on the reconstructed image

A significant drawback of emission tomography is the reduction in the number of radiating isotopes with time, which directly limits the measurement period. In SPECT measurements, the amount of isotopes inserted into the body is limited by health restrictions. This limits the exposure time of the images taken, which in turn reduces the signal. The signal is further lowered by the collimators installed on the detectors. Such limited signal power requires special attention to the noise. It can be shown that by adding white noise to the projections, the standard deviation of the reconstructed image is given by:

$$\sigma^2 = \pi S_0 \int_{-\infty}^{\infty} |w|^2 |G(w)|^2 dw \tag{10}$$

where S_0 is the square of the noise amplitude and *G(w)* is a smoothing filter that has to be chosen. A cutoff frequency will prevent the divergence of the integral. This relation shows that in order to reduce the effect of the noise we should choose a filter such that the

area under the function $|w||G(w)|$ will be as small as possible. On the other hand, from the reconstruction integral (not shown) it appears that $|w||G(w)|$ should be as close to $|w|$ as possible, in order to avoid image distortions. This tradeoff between distortion and noise has to be examined carefully while taking into account the noise amplitude and optical abberations of the system.

2.7 Overview of particle tracking and discretizaiton errors

Microscopic particles are used in a wide range of experiments to monitor the dynamics of objects that cannot be directly visualized. Such particles are also used as tracers in flows or as microprobe for various environments. Quite often these particles are spherical beads of sizes raging between $0.1\mu m$ to several μm. Quite a few tracking algorithms have been used in experiments without a full understanding with regards to their accuracy. In video tracking there are several sources of errors. It is customary to divide the errors in two categories: random and systematic. Random errors (noise) are referred to as limiting the 'precision' of the method while systematic ones (bias) affect the 'accuracy'. While each experimental system has its own characteristics, there is one source of bias that is generic, namely, the bias due to the digitization of the image, $\mathbf{b}$.

In our work we described the behavior of the discretization bias and we have shown that it can be significantly reduced (see section 4). For this purpose we developed an algorithm that allows to track symmetric particles with sub-pixel accuracy, the Symmetry Algorithm. This symmetry algorithm includes a new feature, namely, interpolation. We show that the discretization bias, b, is composed of two parts that to a good approximation are additive. That is, the bias due to the intensity discretization itself, $\mathbf{b}_D$, and that due to interpolation, $\mathbf{b}_I$. Asymptotically, $\mathbf{b}_D \propto N^{-1}N_1^{\frac{1}{2}}$, where N is the number of gray levels and N_1 is the number of pixels in half of the image of the symmetric particle (see Fig. 15). Moreover, in the case of linear interpolation, $\mathbf{b}_I \propto N_e^2 g(\epsilon)$ where N_e is the number of extrema of the intensity function, ϵ is the displacement of the bead center with respect to the pixel center and $g(\epsilon)$ is an antisymmetric function that is almost entirely independent on the intensity function of the particle image, as shown in Fig. 16.

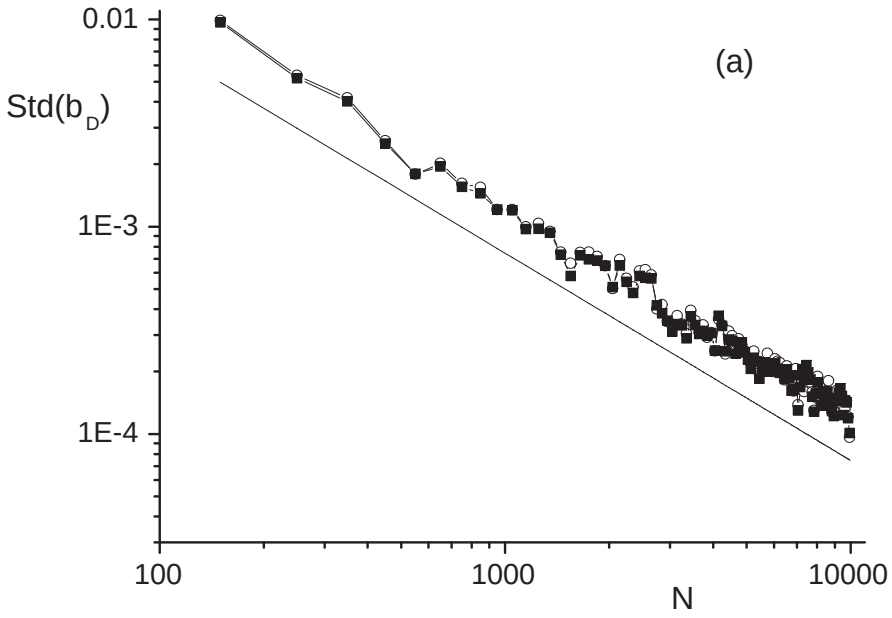

FIG. 15: Variation of b_D as a function of the number of grey levels, N, using either linear (circles) or spline (squares) interpolation for a Gaussian with $\sigma = 10$. The straight line represents our theoretical predictions.

3. Research proposal

This research proposal is focused on applying SPECT which is conventionally used on macroscopic human organs to microscopical objects in order to observe protein 3D structures and their dynamics within single *E. coli* cells. Several technical modifications of the SPECT setup are necessary. First, a microscope is introduced into the system in order to observe the micron sized objects that are being studied. Next, instead of radioactive isotopes, our light source consists of specific fluorophores that are attached to particular proteins. The molecular absorption of fluorophores triggers the emission of another photon with a longer wavelength. The emitted radiation is collected by the microscope objective lens, and is then imaged by a CCD camera. The small dimensions of cells presents an additional complication. While in SPECT imaging the dimensions of the imaged object are usually larger by several orders of magnitude than the wave length of the emitted photons, our objects will be close to the optical resolution limit, as often happens in light microscopy. For example, the dimension of a bacteria is $\sim 3\mu m$ while a typical fluorescent photon wavelength is $\sim 0.5\mu m$. Thus resolution has to be carefully examined and treated, as discussed in section 2.5. Another

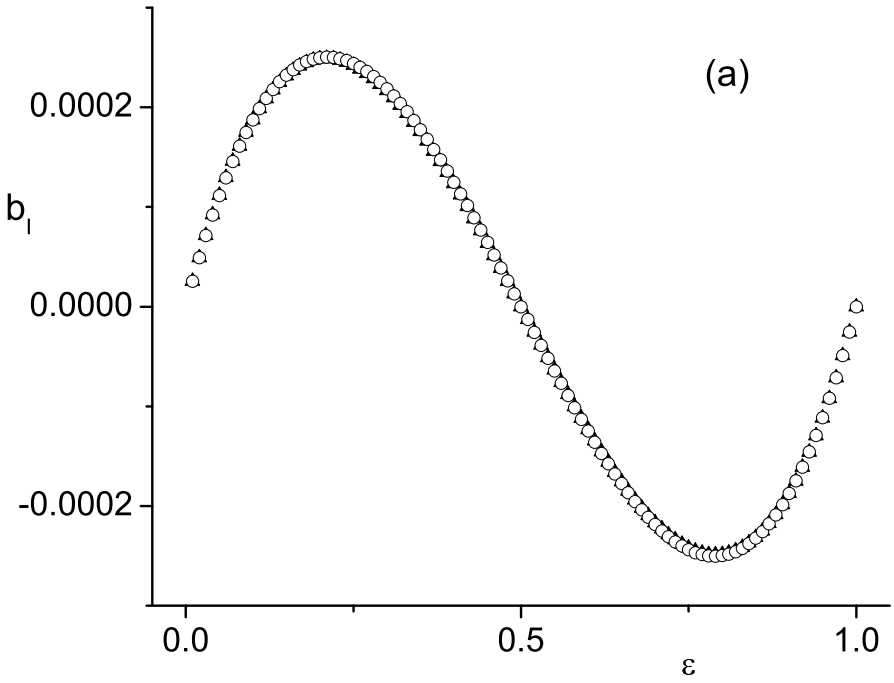

FIG. 16: Variation of b_I as a function of ϵ, the displacement of the bead center with respect to the pixel center, using linear interpolation for a Gaussian with $\sigma = 10$ (circles), a decaying cosine (pluses) and a cosine (triangles). The value of b_I for the decaying cosine and the cosine functions have been normalized such that they are equal to those of the Gaussian at $\epsilon = 0.1$. The reason that only one kind of symbols (circles) is seen is that the others that are of the same size are almost precisely covered by the circles.

fundamental difference between our microscopic SPECT and regular SPECT is that we can not rotate the sensors array while the object remains static. Instead, we rotate the bacteria while the imaging system remains fixed. For this purpose we developed a technique that enables the control of trapped elongated objects orientation (see section 2.2). In addition to the alignment of bacteria, in order to perform tomography reconstruction, the angle of alignment has to be determined. A method was developed for this purpose and is described in section 2.2. Our technique represents an alternative to current methods that provide three dimensional images. The method we propose to obtain 3D images has some advantages over other approaches that were discussed in section 1.2. First, no scanning of the XY plane is needed, which should improve time resolution. Second, the trapped object is suspended in solution, rather than being placed or tethered to the sample glass. This will help avoiding

optical reflections from the cover glass and altering the bacteria natural growing conditions.

The objectives of this study are as follows:

1. To determine the number of division proteins subunits in the divisome.
2. To characterize the divisome proteins configuration and in particular the distribution of the protein structures along the Z-ring.
3. To examine the relation between the MinD and MreB helical structures.
4. To characterize the MinD dynamic mechanism in the polar zone and in the opposite half of the cell.

4. Appendix

Particle tracking and discretizaiton errors

4.1 Introduction

Microscopic particles are used in a wide range of experiments to monitor the dynamics of objects that cannot be directly visualized. Such particles are also used as tracers in flows or as microprobe for various environments. Quite often these particles are spherical beads of sizes raging between $0.1\mu m$ up to several μm. For example, attaching a bead to a single kinesin molecule Sheetz et *al.* [50] monitored its motion along a microtubule. For this purpose, they have developed a sub-pixel video tracking method that uses the correlation function between the images in the different frames. The precision was estimated to be of about $2nm$ corresponding to about 1/40 of the pixel size.

An alternative approach relies on fluorescent particles or dyes. Tracking single fluorophores has allowed to monitor the dynamics of biomolecules in the cell membrane [51–53], in model membranes [54, 55], in solution [56] and inside cells [57]. This field was reviewed in Refs. [58, 59]. Recently, the motion of myosin V on actin was studied using single fluorophores bound to the kinesin molecules [60]. Special care was required in order to prevent the fluorophore from bleaching and to optimize the signal to noise ratio (S/N). The tracking was done using a Gaussian fit to the intensity profile leading to $1.5nm$ precision.

Quite a few tracking algorithms have been used in experiments without a full understanding with regards to their accuracy. The performance of four different tracking algorithms was compared by Cheezum *et al.* [61]. cross-correlation [50, 62, 63], sum-absolute difference [64], centroid [53, 65] and direct Gaussian fit [55, 66] algorithms and have shown the way

in which the various sources of error contribute to the accuracy of the different techniques. The study of Ref. [61] was focused on finding the best way to monitor the dynamics of a single fluorophore. It found that, due to the large S/N, the Gaussian fit is the most accurate algorithm for such experiments. For the case of microscopic particles that are larger than the point-spread function (PSF), they found that the cross-correlation method is the most accurate.

In video tracking there are several sources of error. It is customary to divide the errors in two categories: random and systematic. Random errors (noise) are referred to as limiting the 'precision' of the method while systematic ones (bias) affect the 'accuracy'. Although noise can be reduced by averaging, this limits the time resolution. Even in experiments where this is not an issue, averaging is limited by the stability of the system. On the other hand, one expects that a better understanding of the experimental system would allow to eliminate, or at least reduce the bias. While each experimental system has its own characteristics, there is one source of bias that is generic, namely, the bias due to the digitization of the image, **b**. The purpose of this study is to describe the behavior of the discretization bias and to show how it can be significantly reduced. For this we choose to use a simple algorithm that allows to track symmetric particles with sub-pixel accuracy, the symmetry algorithm. We show that the discretization bias, b, is composed of two parts that to a good approximation are additive, namely, the bias due to the intensity discretization itself, $\mathbf{b}_D$, and that due to interpolation, $\mathbf{b}_I$. Asymptotically, $\mathbf{b}_D \propto N^{-1}N_1^{\frac{1}{2}}$, where N is the number of gray levels and N_1 is the number of pixels in half of the image of the symmetric particle. Moreover, in the case of linear interpolation, $\mathbf{b}_I \propto N_e^2 g(\epsilon)$ where N_e is the number of extrema of the intensity function and $g(\epsilon)$ is an antisymmetric function that is almost entirely independent on the intensity function of the particle image.

4.2 The symmetry algorithm

In the case of both microscopic beads that are larger than the PSF and point sources the ideal image has circular symmetry. This symmetry can be used to find the center of the particle using the lines of symmetry in both the x and y directions, $L_x : y = y_0$ and $L_y : x = x_0$. The center of the particle lies at the intersection of the two symmetry lines, (x_0, y_0). Each of the symmetry lines is found by searching for the minimum of the asymmetry functions, $S_y(\epsilon_x)$ and $S_x(\epsilon_y)$, where ϵ_x and ϵ_y generate sub-pixel shifts of the symmetry center

in the x and y direction respectively. For the case of L_y,

$$S_y(\epsilon_x) = \sum_{i=1}^{N_1} \sum_{j=-N_1}^{N_1} |f(i,j,\epsilon_x) - f(-i,j,\epsilon_x)| \ , \tag{11}$$

where i runs over the pixels to the right of L_y, excluding the $i = 0$ pixels, namely, the pixels through which L_y passes, j runs along the columns of the entire image and $f(i,j,\epsilon_x)$ is the intensity value at $(i - \epsilon_x, y)$. Since digital images only provide intensities of entire pixels, we obtain the value of $f(i,j,\epsilon_x)$ by interpolation between the values of adjacent pixels. In this work, two types of interpolation were used: linear and spline. While linear interpolation is more analytically tractable, the spline interpolation leads to very small values of the corresponding bias, $\mathbf{b}_I$. S_x is obtained by exchanging the roles of i and j and of x and y in Eq. (11).

For a perfectly symmetric intensity function whose values are known at all (x, y) points (no pixels), the minimum of S_x and S_y corresponds to the exact center. However, in actual images the symmetry is weakly perturbed due to optical aberrations, noise and discretization effects. Assuming an ideal optical system that preserves the circular symmetry and ignoring the effect of experimental noise, we are left with the bias that is due to discretization, $\mathbf{b}$. It is defined as

$$\mathbf{b} = \overline{\epsilon}_1 - \overline{\epsilon}_0 \ , \tag{12}$$

where $\overline{\epsilon}_1$ is the measured shift obtained from the minimization of the experimentally measured, discretized S's and $\overline{\epsilon}_0$ gives the position of the true symmetry center of the particle. In the next section, we analyze the behavior of the bias for various types of intensity functions.

4.3 The one-dimensional case

In order to illustrate the behavior of the bias we use three symmetric functions, f_1, f_2, and f_3, where the first is a Gaussian, the second is an exponent that decays in an oscillatory manner and the third is a cosine,

$$f_1(x) = \exp\left(-\frac{x^2}{2\sigma^2}\right) \ , \tag{13}$$

$$f_2(x) = \exp\left(-\frac{|x|}{a}\right) \cos\left[\frac{2\pi x(n+1/2)}{A}\right] \ , \tag{14}$$

$$f_3(x) = \cos\left[\frac{2\pi x(n+c/2)}{A}\right] \ . \tag{15}$$

While the Gaussian represents a good approximation to the PSF, f_2 and f_3 are reminiscent of the images of defocused beads that display multiple interference fringes. We perform on these functions a discretization similar to that of a noise-less one dimensional digital camera with N gray levels and $2N_1 + 1$ pixels.

In a digital CCD the value of the intensity function in a given pixel results from integrating the light intensity over the active area of the pixel. We simplify the process by taking the value of the intensity function at the center of the pixel. The pixels are chosen to be of unit length and centered on integers, such that, in the first digitization step, D_1,

$$D_1 : f_l(x) \rightarrow f_l(i) \ , \tag{16}$$

where $l = 1, 2, 3$ and $-N_1 \leq i \leq N_1$. The second digitization step, D_2, approximates the intensity of the pixel by the closest available gray level,

$$D_2 : f_l(i) \rightarrow \tilde{f}_l(i) \ , \tag{17}$$

where $\tilde{f}_l(i) = \mathrm{fix}[f_l(i)]$ and the function fix rounds the value of $f_l(i)$ to the integer value after the function has been stretched to cover the entire dynamical range between 0 and N. Since the functions we study are symmetric and their symmetry center is at the middle of the central pixel, $i = 0$, the symmetry is preserved under discretization, D, where $D = D_2 \cdot D_1$. We shift the image by $\epsilon_0 \leq 1$ from the origin, $T_{\epsilon_0} : f(x) \rightarrow f(x - \epsilon_0)$ and only then discretize using the operator D, $\tilde{f}_l(i, \epsilon_0) = D \cdot T_{\epsilon_0} f_l(x)$. Due to the mismatch between the pixel array and the symmetry center, the discretization will perturb the symmetry of the function such that $\tilde{f}_l(i, \epsilon_0)$ is only approximatively symmetric. As a consequence, searching for ϵ_0 using the symmetry algorithm of Sec. 4.2 will lead to a slightly different value, ϵ_1. The bias is defined as in Eq. 12, $b = \epsilon_1 - \epsilon_0$. In what follows, we study the behavior of the bias as the various parameters of the problem change, namely, the number of gray levels, N, the number of pixels, N_1 and the various parameters of the intensity functions, $f_l(x)$.

4.4 Dependence of b on N

In what follows, we express all lengths in units of pixels. In Fig.17 and Fig.18 we show the behavior of b for f_1 and f_2 as a function of N for a particular shift $\epsilon_0 = 0.1$ and linear interpolation. For both functions the bias oscillates wildly. However, while for the Gaussian it seems to oscillate around zero, in the case of f_2 it clearly has a finite average value. In fact, the average of b in Fig.17 is $< b_{1,L} >= 1.81 \cdot 10^{-4}$ and in Fig.18 it is

$< b_{2,L} >= 4.66 \cdot 10^{-3}$. When the same calculation is made with spline interpolation the oscillations appear to be quite similar in size but the corresponding averages are different, namely, $< b_{1,S} >= -1.97 \cdot 10^{-5}$ and $< b_{2,S} >= -2.08 \cdot 10^{-4}$. This suggests that the fluctuations in the bias are determined by the D_2 operator which transforms the function into its approximation in terms of N gray levels while the average bias is due to the interpolation. To verify this assumption, we can, in our computation, turn off the D_2 step to obtain a bias that is due to the interpolation alone, b_I. Indeed, for the case of the linear interpolation the values of b_I that we obtain are similar to those of the corresponding $< b >$. Specifically, $b_{I,1,L} = 1.87 \cdot 10^{-4}$, $b_{I,2,L} = 4.00 \cdot 10^{-3}$, where the second index indicates for which function this was calculated and the third which type of interpolation was used (L =linear, S =spline). However, for the case of the spline interpolations, the values of b_I that we find are completely different than those of b_I, that is, $b_{I,1,S} = 1.36 \cdot 10^{-7}$ and $b_{I,2,S} = -1.18 \cdot 10^{-6}$. The discrepancies between $< b >$ and b_I are due to the finite size averaging of $< b >$. These are relatively small for large b_I as is the case for the linear interpolation, but become very large for the spline case. Performing the average of b at large values of N we obtain values that are closer to those of b_I. In particular, when b is averaged over $10^7 \leq N \leq 1.0001 \cdot 10^7$ we obtain $< b_{1,L} >= 1.87 \cdot 10^{-4}$, $< b_{2,L} >= 4.01 \cdot 10^{-4}$, $< b_{1,S} >= 1.87 \cdot 10^{-7}$ and $< b_{2,S} >= -1.36 \cdot 10^{-6}$ showing clear convergence towards the corresponding b_I's. This indicates that the average bias is due to the interpolation error while the fluctuations around this average are due to the discretization error and that one can approximatively decompose b, such that,

$$b \cong b_I + b_D \ , \tag{18}$$

where b_D is the bias that is due to the D_2 operator. In our algorithm the interpolation is performed after the discretization step and therefore its result depends on that of the interpolation. This leads to some coupling between the b_I and b_D and to the approximate equality sign in Eq. (18).

We notice that the magnitude of b_D seems to behave similarly for both types of interpolation.

4.5 Dependence of b_D on N

Treating b_D as an independent entity we show that its behavior can be statistically described to a good approximation. The values of an arbitrary function are unrelated to the gray levels imposed by the camera. It is therefore a reasonable assumption that, on

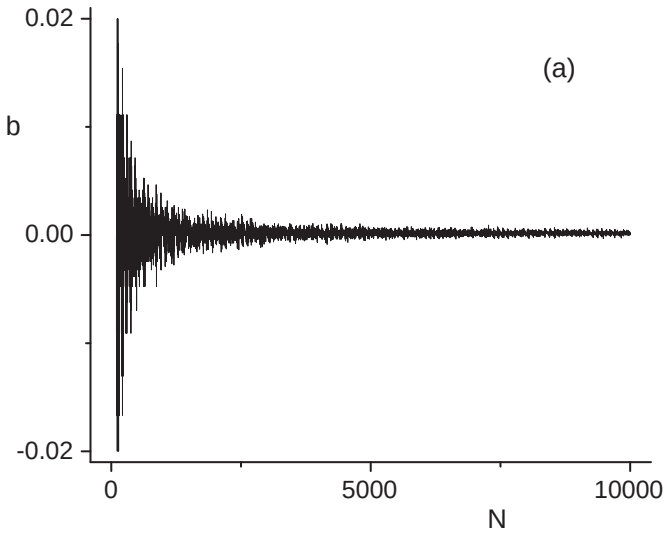

FIG. 17: Variation of the bias as a function of the number of grey levels, N, using linear interpolation for $N_1 = 40$ Gaussian, f_1, with $\sigma = 10$

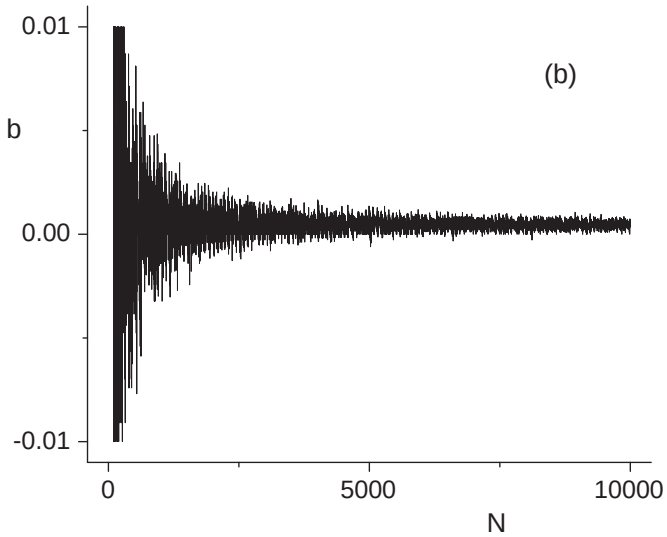

FIG. 18: Same as Fig.17 for a decaying exponent, f_2, with $a = 10$, $A = 40$ and $n = 2$

average, these values are homogeneously distributed between each two adjacent gray levels. One expects that this picture becomes more accurate as N increases. This assumption can be used to obtain an estimate of the asymmetry function of Eq. (11) for a particular value of N, $S_D(N)$. Using this asymmetry value, we approximate the behavior of the corresponding bias. To estimate S, we use a further simplification of the asymmetry algorithm. Instead

of shifting the intensity function, we assume that the discretization errors in the opposite pixels, i-th and $-i$-th, are uncorrelated. Estimating the resulting asymmetry we then obtain the shift required in order to reduce it to a minimal value.

Let Δf_i denote the error in the function due to discretization in pixel number i. Then, if $f_i = f_{-i}$,

$$S_D = \sum_{i=1}^{N_1} \mid \Delta f_i - \Delta f_{-i} \mid \ . \tag{19}$$

If Δf_i are random variables uniformly distributed in $(-a, a)$, where $a = 1/2N$, then

$$<\mid \Delta f_i - \Delta f_{-i} \mid>= \frac{2}{3}a \ , \tag{20}$$

and

$$< S_D >= \frac{2N_1}{3}\frac{f(0)}{2N} \ . \tag{21}$$

Similarly, we can calculate the standard deviation of S_D, $Std(S_D)$. However, $Std(S_D)$ also depends on the correlations between Δf_i and Δf_j. For the lowest order approximation, we assume that $< \Delta f_i \Delta f_j >=< \Delta f_i >< \Delta f_j >$. Then,

$$Std(S_D) \simeq \frac{\sqrt{2N_1}}{3}\frac{f(0)}{2N} \ . \tag{22}$$

We can now relate the estimated asymmetry value, S_D, to a correspondingly approximated value of the discretization bias, b_D. For this we calculate the degree of asymmetry, S, resulting from translating a symmetric function, f. The asymmetry is measured with respect to the original center of symmetry. For simplicity, we consider the continuous case over the entire $(-\infty, \infty)$ interval. Moreover, we approximate S by a simpler expression, S_1, which is the same as that of Eq. (11) only without the absolute value. Clearly, $S_1 \leq S$ and equality is obtained for functions monotonic in $(0, \infty)$. For small translations, T_ϵ, where $\epsilon \to 0$,

$$S_1 = 2f(0)\epsilon \ . \tag{23}$$

Using this result in Eq. (22) we obtain

$$Std(b_D) \sim \frac{\sqrt{2N_1}}{12N} \ , \tag{24}$$

where $\sim$ indicates that due to the several approximations this should be regarded as no more than an estimate. In Fig.19 and Fig.20 we test the validity of Eq. (24) for the case of f_1 and f_2. Here the value of b_D is obtained from Eq. (18) where b_I is computed by turning off discretization and the approximate equality is assumed to be exact. The standard deviation

of b_D is computed by averaging over consecutive intervals of N of 10^2. Notice that for both functions $Std(b_D) \simeq \alpha N^{-1}$ where α is larger than the theoretical prediction of Eq. (24), $\alpha_T = \frac{\sqrt{2N_1}}{12}$ by a factor, R_α, that was found numerically to range between 1 and 2. One reason for which $R_\alpha > 1$ is that a positive quantity, namely, the correlations, were assumed to vanish in the derivation of Eq. (24). Another source of discrepancy between theory and numerics, that however works in the opposite direction, is due to the effective number of pixels, N_1, that is used in Eq. (24). This problem is particularly important for the case of the Gaussian, f_1. Since it is a rapidly decaying function, for $\sigma = 10$, the values of f_1 in the pixels $\mid i \mid \geq 37$ are small and will be discretized to zero for all the values of N shown in Fig. 1a. For smaller N's, the values of the function in these pixels are too small to produce a significant contribution to the discretization error and therefore, the effective value of N_1 is both smaller than 40 and its size depends on N.

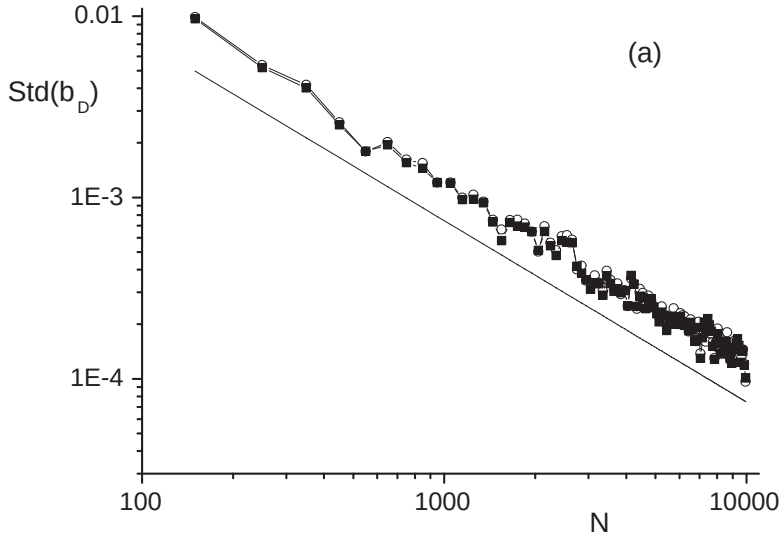

FIG. 19: Variation of the bias as a function of the number of grey levels, N, using linear interpolation for $N_1 = 40$ Gaussian, f_1, with $\sigma = 10$

On the other hand, computing the average of b_D, $< b_D >$, in the same way as $Std(b_D)$, we find a different behavior from that predicted by Eq. (21). Specifically, $< b_D >$ simply fluctuates around zero. This is due to the difference between the actual calculation required by the symmetry algorithm and our simplified version used for deriving the analytical approximations of Eqs. (21) and (22). In the simplified algorithm, the finite $< S_D >$ is due to averaging over a positive definite quantity. On the other hand, in the full symmetry

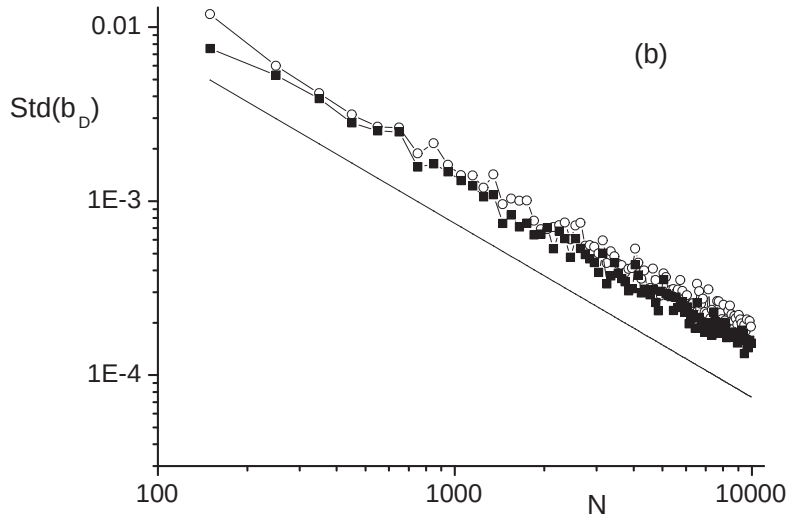

FIG. 20: Same as Fig.19 for a decaying exponent, f_2, with $a = 10$, $A = 40$ and $n = 2$

algorithm the restoring shift, ϵ_1, will be such as to compensate a finite $< S_D >$.

4.6 Dependence of b_I on ϵ

For practical purposes, the most important fact concerning the interpolation bias, b_I, is that when using spline interpolation it becomes so small (see Sec. 4.4) that it is negligible. For example, for the quite extreme case of f_2 with the parameters of Fig.18, only CCD's with more than 19 bit/pixel would reach the range where $b_{I,S,2} \sim b_D$. Moreover, in most applications such low levels of discretization errors are most likely negligible relative to the other sources of error, e.g. noise. On the other hand, since spline interpolation is a computationally expensive method it is worthwhile to understand the behavior of b_I for the case of the linear interpolation.

The interpolation bias, b_I depends on the value of ϵ. In Fig.16 we show that $b_I \propto g(\epsilon)$ where $g(\epsilon)$ is practically independent of the form of the intensity function. From the definition of the asymmetry function, Eq. (11), it can be shown that $g(\epsilon)$ is antisymmetric, $g(\epsilon) = g(-\epsilon)$.

It is important to point out that the minima of the asymmetry function, $S(\epsilon)$, of Eq. (11), is of not the usual quadratic type when using linear interpolation. Instead, the minima are non-differentiable corners that are due to the absolute value function in the definition of $S(\epsilon)$. Each term in the sum of Eq. (11) reaches a minimal value at a particular value of

ϵ, ϵ_i, where the corresponding pair of pixels, i and $-i$, contribute equally. On both sides of ϵ_i, the i-th term depends linearly on ϵ. As a result, $S(\epsilon)$ is composed of linear segments that change slope discontinuously at ϵ_i. It is one of the terms of the sum, i_m, which in fact determines the position of the minimum, ϵ_{i_m}. Continuously modifying the intensity function, f, for example, by changing one of its parameters, leads to points where the value of i_m changes, that is, a new pair of pixels determines the position of the minimum. At such points in parameter space, the value of b_I changes discontinuously (see Fig.21). The size of the discontinuity is determined by the difference between the adjacent ϵ_i's. As the number of pixels that contribute to $S(\epsilon)$ grows, the ϵ_i's grow denser and the corresponding jumps in b_I get smaller. In the limit of small number of pixels however, the discontinuous jumps will dominate the quantitative behavior of b_I. Notice that the fact that jumps occur at equidistant values of σ is particular to the case of the Gaussian. For the decaying cosine, f_2, the jumps appear in a complex pattern when the value of A is varied. Clearly, further work is required in order to fully understand the relation between the intensity function and the pattern of these discontinuities in b_I. Another feature of the $b_I(\sigma)$ of Fig.21 is that, overall, it decreases as σ grows. Qualitatively, this is due to improved averaging as more pixels participate in determining the behavior of $S(\epsilon)$.

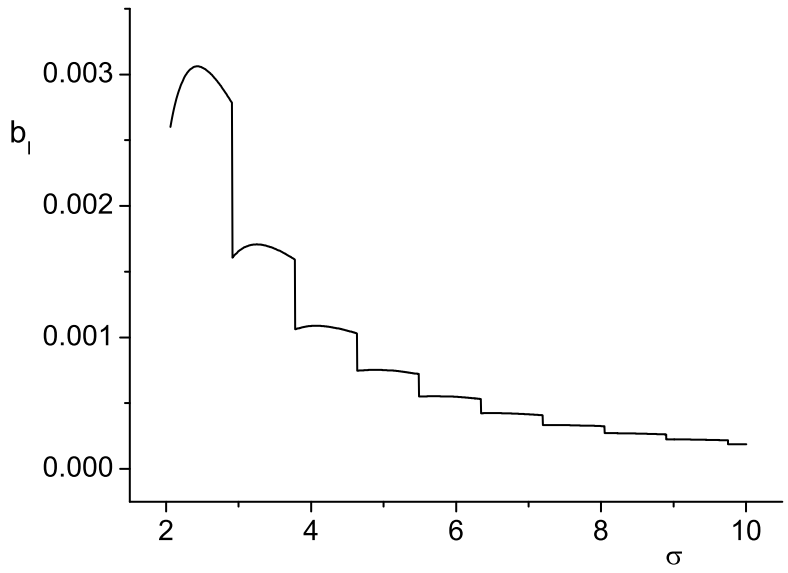

FIG. 21: Variation of b_I as a function of a parameter of the intensity function for the case of the Gaussian, f_1, where we change its width, σ, for linear interpolation, $\epsilon = 0.1$ and $N_1 = 40$.

4.7 The two-dimensional case

Several aspects of the behavior of the bias have not been discussed in detail in Sec. 4.3. The main issue is the extension of our analysis to the two-dimensional (2D) case. We find that all our findings directly generalize to 2D for objects with circular symmetry. Each of the components of $\mathbf{b}$, b_x and b_y, behave analogously to the one-dimensional b. The standard deviation of the discretization bias, b_D, is overestimated by Eq. (24) by a similar factor only that now the number of pixels, N_1, is significantly larger. Also in 2D, b_I is negligible when spline interpolation is used and behaves similarly to what was found in 1D as a function of N_E and ϵ.

4.8 Discussion and conclusions

An experimental verification of our predictions will require special care in order to separate the bias due to discretization from the other sources of error. The system should have low noise and drift levels such that using time-averaging one can reduce the effective noise to a range that is significantly below the bias due to discretization, $\|\mathbf{b}\|$. In such a system and if the sample can be rotated around the optical axis with an error, Δ_R, such that $\Delta_R \ll \|\mathbf{b}\|$, one can separate the total bias, $\mathbf{b_T}$, from the random errors. This approach is standardly used in mask alignment in lithography where $\mathbf{b_T}$ is referred to as *tool induced shift* [67]. However, $\mathbf{b_T}$ contains additional contributions from optical abberations and imperfections of the CCD, e.g. banding, interlace, clock jitter, etc. On the other hand, our predictions regarding the behavior of $\mathbf{b}$ can be used to estimate its size in a particular experiment when the symmetry algorithm is used for position detection. Moreover, for a particular image one can calculate $\mathbf{b}$ and use it to appropriately correct the experimentally measured position.

The symmetry algorithm is conceptually not very different from the other tracking algorithms studied in Ref. [61]. It is therefore natural to expect that some of its features will also manifest in the other algorithms.

[1] K. Svoboda, S.M. Block, Opt. Lett. **19**, 730 (1994).

[2] S.M. Block, L.S.B. Goldstein, B.J. Schnapp, Nature **348**, 348 (1990).

[3] A. Ashkin, K. Schutze, J.M. Dziedzic, U. Eutenauer, and M. Schliwa, Nature **348**, 346 (1990).

[4] Y. Tadir, W.H. Wright, O. Vafa, T. Ord, R.H. Asch, and M.W. Berns, Fertility and Steriligy **52**, 870 (1989).

[5] J.M. Colon, P. Sarcosi, P.G. McGovern, A. Ashkin, J.M. Dziedzic, J. Skurnick, G. Weiss, and E.M.Bonder, Fertility and Steriligy **57**, 695 (1992).

[6] E.M. Bonder, J.M. Colon, J.M. Dziedzic, and A. Ashkin, J. Cell. Biol. **111**, 421 (1990).

[7] M. Kurachi, M. Hoshi, and H. Tashiro, Cell Moitl. Cytoskel. **30**, 221 (1995).

[8] H. Feigner, R. Frank, and M. Schliwa, J. Cell Sci. **109**, 509 (1996).

[9] T. Tsuda, H. Tasutake, A. Ishijima, and T. Yanagida, Proc. Natl. Acad. Sci. USA **93**, 12937 (1996).

[10] T.T. Perkins, D.W. Smith, and S. Chu, Science **264**, 822 (1994).

[11] S.B. Smith, Y. Cui, and C. Bastamante, Science **271**, 795 (1996).

[12] G. Wright, M.J. Tucker, P.C. Morton, C.L. Sweitzer-Yoder, and S.E. Smith, Current Opinion in Obstetrics and Gymecology, **10**, 221 (1998).

[13] J.C. Crocker, and D.G. Grier, Phys. Rev. Lett. **73**, 352 (1994).

[14] A. Choudhury, B.J. Ackerson, and N.A. Clark, Phys. Rev. Lett. **55**, 833 (1985).

[15] A.D. Dinsmore, A.G. Yodh, and D.J. Pine, Nature **383**, 239 (1996).

[16] K. Sasaki, M. Koshio, H. Misawa, N. Kitamura, and H. Masuhara, Opt, Lett. **16**, 1463 (1991).

[17] K. Sasaki, H. Fujiwara, and H. Masuhara, J. Vacuum Sci. Tech. B **15**, 2786 (1997).

[18] K. Visscher, G.J. Brakenhoff, and J.J. Krol, Cytometry, **14**, 95 (1993).

[19] V. Bingelyte, J. Leach, J. Courtial, and M.J. Padgett, App. Phys. Lett. **82**, 829 (2003).

[20] M.E.J. Friese, T.A. Nieminen, N.R. Heckenberg, and H. Rubinsztein-Dunlop, Nature **395**, 621 (1998).

[21] A.T. O'Neil, and M.J. Padjett, Opt. Lett. **27**, 743 (2001).

[22] L. Paterson, M.P. MacDonald, J. Arlt, W. Sibbett, P.E. Bryant, K. Dholakia, Science **292**, 912 (2001).

[23] E. Higurashi, R. Sawada, and T. Ito, J. Micromech. and Microeng. **11**, 140 (2001).

[24] M.E.J Friese, T.A. Nieminen, N.R. Hekenberg, and H. Rubinsztein-Dunlop, Opt. Lett. **23**, 1

(1998).

[25] J.A. Dharmadhikari, and D. Mathur, Curr. Sci. **86**, 1432 (2004).

[26] G. Nomarski, J. Phys. Radium **16**, 9 (1955).

[27] W. Denk, J.H. Strickler, Science **248**, 73 (1990).

[28] J. Lutkenhaus, S.G. Addinall, Annu. Rev. Biochem **66**, 93 (1997).

[29] X. Ma, D.W. Ehrhardt, W. Margolin, Proc. Natl. Acad. Sci. USA **93**, 12998 (1996).

[30] J.C. Chen, D.S. Weiss, J.M. Chigo, J. Beckwith, J. Bacteriol. **181**, 521 (1999).

[31] D. Joseleau-Petit, D. Vinella, and R. D'ari, J. Bacteriol **181** 9, (1999).

[32] H.P. Erickson, D.W. Taylor, K.A. Taylor, and D. Branmhill, Proc. Natl. Acad. Sci. **93**, 519 (1996).

[33] J. Stricker, P. Maddox, E.D. Salmon, and H.P. Erickson, Microbioloty **99**, 3171 (2002).

[34] M. Vicente, A.I. Rico, R.M. Arteaga, and J. Mingorance, J. Bacterio. **188**, 19 (2006).

[35] Y.L. Shih, T. Le, and L. Rothfield, Cytometry **100**, 7865 (2003).

[36] S. Tamaki, H, Matzusawa, and M. Matsuhashi, J. Bacteriol. **141**, 52.

[37] G. Carmon, N. Mamman, and M. Feingold, Physica A **376**, 117 (2007).

[38] A. Ashkin, Opt. Lett. **11**, 288 (1986).

[39] A. Ashkin, Phys. Rev. Lett. **24**, 146 (1970).

[40] A. Ashkin, J. M. Dziedzic, and T. Yamane, Nature (London) **330**, 769 (1987).

[41] R. C. Gauthier, J. Opt. Soc. Am. B **14**, 3323 (1997).

[42] R. C. Gauthier, M. Ashman, and C.P. Grover, Appl. Opt. **38**, 4861 (1999).

[43] H. Nyquist, Trans. AIEE **47**, 617 (1928).

[44] C. E. Shannon, Bell Syst. Tech. J. **27**, 379 (1948).

[45] S. Bellini, M. Pianentini and P. L. De Vinci, IEEE Trans. Acoust. Speech Signal Processing, **ASSP-27**, 213 (1979).

[46] M. Hayashi, J Deguchi, K. Utsunomiya, M. Yamada, T. Komori, M. Takeuchi, K. Kanna and I. Narabayashi, Nucl. Med. Technol **33**, 224 (2005).

[47] L. T. Chang IEEE Trans. Nucl. Sci. **26**, 2780 (1979).

[48] K. Ogawa, Y. Harata, T. Ichihara, A. Kubo and S. Hashimoto, IEEE Trans. Med. Imaging **10**, 3 (1991).

[49] O. J. Tretiak and T. Metz, Siam J. Apll. Math. **39**, 341 (1980).

[50] J. Gelles, B.J. Schnapp, and M.P. Sheetz, Nature **331**, 450 (1988).

[51] L.S. Barak, and W.W. Webb, J. Cell Biol. **98**, 595 (1981).

[52] D. Gross, and W.W. Webb, Biophys. J. **49**, 901 (1986).

[53] R.N. Ghosh, and and W.W. Webb, Biophys. J. **66**, 1301 (1994).

[54] T. Schmidt, G.J. Schutz, W. Baumgartner, H.J. Gruber, and H. Schindler, Proc. Natl. Acad. Sci. U.S.A. **93**, 2926 (1996).

[55] G.J. Schutz, H. Schindler, and T. Schmidt, Biophys. J. **73**, 1073 (1987).

[56] U. Kubitscheck, O. Kuckmann, T. Kues, and R. Peters, Biophys. J. **78**, 2170 (2000).

[57] M. Goulian, and S.M. Simon, Biophys. J. **79**, 2188 (2000).

[58] M.J. Saxton, and K. Jacobson, Annu. Rev. Biophys. Biomol. Struct. **26**, 373 (1997).

[59] R.J. Cherry, P.R. Smith, I.E. Morrison, and N. Fernandez, FEBS Lett. **430**, 88 (1998).

[60] A. Yildiz, J.N. Forkey, S.A. McKinney, T. Ha, Y.E. Goldman, and P.R. Selvin, Science **300**, 2061 (2003).

[61] M.K. Cheezum, W.F. Walker, and W.H. Gullford, Biophys. J. **81**, 2378 (2001).

[62] A. Kusumi, Y. Sako, and M. Yamamoto, Biophys. J. **65**, 2021 (1993).

[63] W.H. Guilford, and R.W. Gore, Microvas. Res. **50**, 260 (1995).

[64] L.N. Bohs, B.H. Friemel, B.A. McDermott, and G.E. Trahey, Ultrasound Med. Biol. **19**, 751 (1993).

[65] G.M. Lee, A. Ishihara, and K.A. Jacobson, Proc. Natl. Acad. Sci. U.S.A. **88**, 6274 (1991).

[66] C.M. Anderson, G.N. Georgiou, I.E.G. Morrison, G.V.W. Stevenson, and R.J. Cherry, J. Cell. Sci. **101**, 415 (1992).

[67] T.C. Rigden, A.J. Soroka, and L.A. Binns, preprint (2005).